Earth Planet. Sci. Lett. 656 (2025) 119277

Contents lists available at ScienceDirect

Earth and Planetary Science Letters

journal homepage: www.elsevier.com/locate/epsl

The partitioning of selenium and tellurium between sulfide liquid and silicate melt and their abundances in the silicate Earth

Zhiwei Liu [a,b], Yuan Li [b,*]

[a] State Key Laboratory of Deep Earth Processes and Resources, Guangzhou Institute of Geochemistry, Chinese Academy of Sciences, 510640 Guangzhou, China
[b] Bayerisches Geoinstitut, Universität Bayreuth, 95440 Bayreuth, Germany

ARTICLE INFO

Editor: DR J BADRO

Keywords:
Se and Te
Sulfide liquid
Silicate melt
Partition coefficient
Morbs
Silicate earth

ABSTRACT

Near-chondritic relative abundances of sulfur (S), selenium (Se), and tellurium (Te) observed in mantle peridotites have been used to support the hypothesis of a carbonaceous chondrite-like late veneer added to the proto-Earth. However, the extent to which the observed S, Se, and Te compositions represent the signature of the silicate Earth remains a topic of debate. The concentrations of Se and Te in mantle-derived melts, such as mid-ocean ridge basalts (MORBs), can help clarify this issue, provided we have a precise understanding of the behavior of Se and Te during magmatic differentiation and mantle partial melting. Here we conduct laboratory experiments to determine the sulfide liquid–silicate melt partition coefficients of Se and Te ($D^{Sul/Sil}_{Se,\ Te}$) at crust–mantle conditions. Our results indicate that $D^{Sul/Sil}_{Se,\ Te}$ range from 180 to 2200 for Se and from 1000 to 25,400 for Te, exhibiting an inverted U-shaped dependence on the FeO_{tot} content in silicate melt. We parameterize $D^{Sul/Sil}_{Se,\ Te}$ as a multi-function of the compositions of silicate melt and sulfide liquid, with pressure (0.5–2.5 GPa), temperature (1273–1973 K), and oxygen fugacity (FMQ-5 to FMQ+1.5; FMQ refers to the fayalite–magnetite–quartz buffer) having negligible effects on $D^{Sul/Sil}_{Se,\ Te}$. Applying our parameterization to magmatic differentiation can effectively account for the Se, Te, and Cu systematics observed in both MORBs and oxidized arc magmas. More significantly, when applied to mantle partial melting, alongside high-precision Se and Te concentration data from MORBs, our parameterization yields superchondritic S/Se, S/Te, and Se/Te ratios in the depleted MORB mantle and primitive mantle, compared to carbonaceous chondrites. These findings suggest that the S, Se, and Te abundances in the silicate Earth were likely established during the main accretion phase, with the late veneer playing only a minor role.

1. Introduction

Like sulfur (S), selenium (Se) and tellurium (Te) are moderately volatile elements and exhibit a strong affinity for iron-rich metallic melts and sulfide liquids (König et al., 2014; Lorand and Alard, 2010; Patten et al., 2013). Therefore, the partition coefficients of Se and Te between metallic melt, sulfide liquid, and silicate melt have been determined to understand their origin and distribution during Earth's accretion and core–mantle–crust differentiation (Brenan, 2015; Kiseeva et al., 2017; Li et al., 2021; Rose-Weston et al., 2009). Based on concentrations and ratios in mantle peridotites, it has long been suggested that S, Se, and Te in the silicate Earth exhibit near-chondritic relative abundances (McDonough and Sun, 1995; Wang and Becker, 2013), with absolute concentrations higher than predicted from core–mantle partitioning (Rose-Weston et al., 2009; Wang and Becker, 2013). This near-chondritic relative abundance suggests that S, Se, and Te in the silicate Earth may have originated from a "late veneer" of unprocessed CI or CM chondrite-like composition, which hypothesis was initially proposed to explain the depleted yet near-chondritic relative abundances of PGEs (platinum group elements) in the silicate Earth (Becker et al., 2006; Walker, 2009). Support for this model includes observations that mantle peridotites and CI chondrites share similar Se isotope compositions, and some terrestrial samples (mantle peridotites, sediments, and ore samples) and CM chondrites share similar Te isotope compositions (Fehr et al., 2018; Hellmann et al., 2021; Varas-Reus et al., 2019). However, mantle peridotites exhibit a Se isotope composition that differs from that of CM chondrites (Varas-Reus et al., 2019), and the Se isotope composition of the depleted MORB mantle (DMM) differs

* Corresponding author.
E-mail address: Yuan.Li@uni-bayreuth.de (Y. Li).

https://doi.org/10.1016/j.epsl.2025.119277
Received 6 November 2024; Received in revised form 6 February 2025; Accepted 17 February 2025
Available online 24 February 2025

from that of CI or CM chondrites (Labidi et al., 2018; Yierpan et al., 2019, 2020). Hellmann et al. (2021) proposed that Se and Te isotopes may undergo alteration due to physical and chemical processes after planetary accretion, which complicates their use as tracers of accretionary sources. Moreover, the silicate Earth displays a subchondritic S isotope composition (Labidi et al., 2013). This subchondritic S composition, along with the specific Se and Te isotope patterns, may reflect signatures of core–mantle segregation in a magma ocean or the accretion of evaporated planetesimals during Earth's main accretion phase, rather than the addition of CI or CM chondrite-like late veneer (Labidi et al., 2013; Suer et al., 2017; Wang et al., 2021, 2023).

The question of whether the near-chondritic relative abundances of S, Se, and Te observed in mantle peridotites truly represent the silicate Earth's composition also remain under debate (König et al., 2014, 2015b; Wang and Becker, 2015b). Some researchers argued that the variations in Se and Te found in mantle peridotites cannot be attributed solely to melting process but rather reflect metasomatic overprinting by Se- and Te-rich sulfides and associated platinum-group minerals (Harvey et al., 2015; König et al., 2014; Luguet et al., 2015). If this is accurate, the near-chondritic S/Se and S/Te ratios observed in mantle peridotites would not represent a primitive signature of Earth's mantle. However, this conclusion was contested by Wang and Becker (2015b), who previously proposed chondritic S, Se, and Te ratios in the silicate Earth (Wang and Becker, 2013). They argued that the correlations between Se, Te, and Al_2O_3 in mantle peridotites provide a reliable basis for estimating Se and Te abundances in the silicate Earth, irrespective of melting depletion or refertilization. Mantle-derived melts, such as mid-ocean ridge basalts (MORBs), sourced from the depleted upper mantle (the residual of primitive mantle after ~2–3 % melt extraction, per Workman and Hart (2005)), may help clarify this debate by offering additional constraints on Se and Te abundances in the silicate Earth—provided the behavior of Se and Te during MORB genesis and differentiation is well understood (Yierpan et al., 2019). Since Se and Te have a strong affinity for sulfides, and sulfide liquids are present during both MORB genesis and differentiation (Jenner et al., 2010; Wang and Becker, 2015a; Zhang and Hirschmann, 2016), the Se and Te concentrations and ratios in MORBs are largely governed by sulfide liquid–silicate melt partitioning. However, accurate sulfide liquid–silicate melt partition coefficients of Se and Te ($D^{Sul/Sil}_{Se,\ Te}$) are currently limited. Brenan (2015) has determined $D^{Sul/Sil}_{Se,\ Te}$ at conditions relevant to mantle partial melting, yet these values do not fully explain the Se, Te, and Cu systematics observed in MORBs or arc magmas (Brenan, 2015; Yierpan et al., 2019). Unpublished $D^{Sul/Sil}_{Se}$ values ranging from 450–850 and $D^{Sul/Sil}_{Se}$ from 2600–3800 for andesite and basalt were reported in Kiseeva et al. (2017). While $D^{Sul/Sil}_{Se,\ Te}$ values have been established for oxidized arc magmas (Li et al., 2021) and highly reduced lunar basalts (Steenstra et al., 2018), their applicability to MORB genesis and differentiation is uncertain, as the effects of temperature and oxygen fugacity (fO_2) on $D^{Sul/Sil}_{Se,\ Te}$ remain unclear.

In this study, we present systematic measurements of $D^{Sul/Sil}_{Se,\ Te}$ at crust–mantle conditions. Our results show that these $D^{Sul/Sil}_{Se,\ Te}$ values can successfully explain the Se, Te, and Cu systematics observed in both MORBs and arc magmas. Using high-precision Se and Te data of MORBs, we apply our $D^{Sul/Sil}_{Se,\ Te}$ values to estimate the Se and Te abundances in the DMM and primitive mantle (PM). Our findings indicate that the silicate Earth may have lower Se and Te abundances than previously estimated and exhibits superchondritic S/Se and S/Te ratios. This suggests that the abundances of S, Se, and Te in the silicate Earth cannot be attributed to the addition of a volatile-rich late veneer.

2. Experimental and analytical methods

We conducted laboratory experiments at 1 GPa, 1200–1600 °C, and fO_2 of ~FMQ-1.6 to FMQ+1.5 (FMQ refers to the fayalite–magnetite–quartz buffer) to examine the effect of temperature, fO_2, and sulfide and silicate melt composition on $D^{Sul/Sil}_{Se,\ Te}$ (Table 1). Starting materials included synthetic sulfides and silicates (details in Supplementary Materials). The sulfides were composed of 40–50 wt.% Fe, 1–10 wt.% Cu, 7–15 wt.% Ni, 36–40 wt.% S, 0.2–0.4 wt.% Se, and 0.3–0.8 wt.% Te, while the silicate composition ranged from basalt to rhyolite (Table S1). In most experiments, mixtures of ~80 wt.% silicate and ~20 wt.% sulfide were loaded into graphite capsules. In one experiment (run DO1), we used a composition of ~60 wt.% silicate, ~20 wt.% sulfide (with ~2 wt.% Se and ~6 wt.% Te), and ~20 wt.% anhydrite in a MgO capsule. This setup was designed for comparison with previous experiments conducted at oxidized arc conditions (Li et al., 2021). In two experiments (runs C-2 and E-1), we added excess FeO to the synthetic basalt to achieve a high FeO content in the resulting basaltic melts. In another two experiments (runs O-1 and O-2), FeS_2 (pyrite) was added alongside synthetic sulfide to reduce the FeO content in the resulting rhyolitic melts, following the reaction: FeS_2 (pyrite) + FeO (silicate) = 2FeS (sulfide liquid) + $1/2O_2$ (gas). For graphite-saturated experiments, the fO_2 values were close to the C–CO_2 buffer (Médard et al., 2008), approximately FMQ-1.6 at our experimental P–T condition. In run DO1, the addition of ~20 wt.% anhydrite raised the fO_2 to around FMQ+1.5 (Li et al., 2021).

All experiments were conducted in an end-loaded, solid-media piston cylinder apparatus, with 3/4-inch diameter talc-Pyrex assemblies and graphite heaters. A friction correction of 18 % was applied to the nominal pressure, based on calibrations from the quartz–coesite and kyanite–sillimanite transitions. The total pressure uncertainty was <0.1 GPa. Temperatures were monitored by S-type ($Pt–Pt_{90}Rh_{10}$) or C-type ($W_{95}Re_{05}$-$W_{74}Re_{26}$) thermocouples with an uncertainty of ~10 °C. All experiments were quenched by turning off the electrical power supplied to the graphite heaters.

The major element compositions of the quenched sulfide liquids and silicate melts were determined by a JEOL JXA-8530F electron microprobe in wavelength-dispersive mode, with ZAF calibration applied to reduce matrix effects. For sulfide liquids, we used an acceleration voltage of 20 kV and a beam current of 20 nA, while silicate melts were analyzed with 15 kV/10 nA settings. A defocused beam with a diameter of 20 μm was used for both sulfide liquid and silicate melt measurements.

The major and trace elements, including Cu, Ni, Se, and Te, in the quenched sulfide liquids and silicate melts were analyzed by laser-ablation ICP–MS, using an Agilent 7900 Quadrupole ICP–MS coupled to a Photon Machines Analyte HE 193-nm ArF Excimer Laser Ablation system. Fig. S1 shows the typical LA–ICP–MS signals of various Se and Te isotopes from our experimental products and reference materials (NIST 612 and BCR-2 G). NIST 610 served as the external standard, while Si and Fe contents determined by EPMA were used as internal standards for silicate melts and sulfide liquids, respectively. The LA–ICP–MS detection limits for Se and Te in silicate melts were ~100–500 ng/g and ~10–60 ng/g, respectively, significantly lower than the measured concentrations of Se and Te in our silicate melts (1.9–19.7 μg/g and 0.3–26.7 μg/g, respectively).

Detailed analytical conditions for EPMA and LA–ICP–MS are provided in the Supplementary Materials. The measured major and trace element concentrations in silicate melts and sulfide liquids are presented in Tables S2 and S3.

3. Results

3.1. Major and trace element compositions of samples

All experimental conditions and products are given in Table 1. Sulfide liquid and silicate melt were present in all experiments (Fig. S2). In run DO1, anhydrite, sulfide liquid, and silicate melt coexisted, with

Table 1
Overview of the experimental conditions and products and the calculated partition coefficients of Se and Te between sulfide liquid and silicate melt.

Exp. ID	Starting materials	T (°C)	P (GPa)	Duration (Hours)	Capsule	Run products	ΔFMQ	S in silicate melt (μg/g)	1σ	$D_{Se}^{Sul/Sil}$	1σ	$D_{Te}^{Sul/Sil}$	1σ	$D_{S}^{Sul/Sil}$	1σ	$D_{Cu}^{Sul/Sil}$	1σ
C-2	Basalt + Sulfide-1 + 10 % FeO	1400	1	24	Graphite	Sil + Sul	< −1.6	3889	317	176	9	1036	94	83	7	256	42
E-1	Basalt + Sulfide-1 + 5 % FeO	1400	1	36	Graphite	Sil + Sul	< −1.6	1802	147	310	18	1682	409	189	16	510	42
C-1	Basalt + Sulfide-1	1400	1	24	Graphite	Sil + Sul	< −1.6	2572	134	333	14	2833	259	131	7	516	40
C-4	Andesite + Sulfide-1	1400	1	24	Graphite	Sil + Sul	< −1.6	881	121	664	39	2531	407	389	54	890	153
C-3	Dacite + Sulfide-1	1400	1	24	Graphite	Sil + Sul	< −1.6	429	72	860	99	7344	3717	774	131	1734	248
C-5	Rhyolite + Sulfide-2	1400	1	24	Graphite	Sil + Sul	< −1.6	499	88	1715	205	25,394	5332	672	119	2614	482
O-2	Rhyolite + Sulfide-2 + 5 % FeS_2	1400	1	24	Graphite	Sil + Sul	< −1.6	815	47	2170	285	21,035	3531	434	26	3901	508
O-1	Rhyolite + Sulfide-2 + 10 % FeS_2	1400	1	24	Graphite	Sil + Sul	< −1.6	1615	54	1690	149	4443	1210	241	8	4207	339
E-2	Basalt + Sulfide-1	1300	1	36	Graphite	Sil + Sul	< −1.6	967	98	308	53	1871	392	345	35	872	24
E-3	Basalt + Sulfide-1	1500	1	24	Graphite	Sil + Sul	< −1.6	2218	107	306	20	1608	423	152	8	436	15
E-4	Basalt + Sulfide-1	1600	1	24	Graphite	Sil + Sul	< −1.6	2775	330	261	6	1759	102	121	15	284	68
E-5	Basalt + Sulfide-3	1500	1	24	Graphite	Sil + Sul	< −1.6	2114	190	397	10	2766	189	155	15	446	86
E-6	Basalt + Sulfide-3	1600	1	24	Graphite	Sil + Sul	< −1.6	2458	246	335	13	2154	212	129	13	354	29
ED-2	Andesite + Sulfide-1	1200	1	48	Graphite	Sil + Sul	< −1.6	328	36	716	44	2695	786	1019	112	1293	227
ED-3	Andesite + Sulfide-1	1300	1	36	Graphite	Sil + Sul	< −1.6	427	60	772	44	2947	266	757	108	1171	231
ED-5	Andesite + Sulfide-2	1500	1	24	Graphite	Sil + Sul	< −1.6	1247	29	869	47	3574	522	277	8	814	126
ED-6	Andesite + Sulfide-3	1500	1	24	Graphite	Sil + Sul	< −1.6	1596	96	610	64	3725	477	193	14	482	60
DO1	Andesite + Sulfide-4 + Anhydrite	1200	1	48	MgO	Sil + Oli + Sul + Anhy	~1.5	1173	83	877	153	2460	159	242	18	1218	200

Sil = quenched silicate melt; Sul = sulfide liquid; Anhy = anhydrite; Oli=olivine.
See Table S1 for the composition of Sulfide-1 to Sulfide-4 used in the starting materials.

small olivine crystals forming due to interactions between the MgO capsule wall and the silicate melt.

The FeO_{tot} content of the silicate melts ranged from 13.88 to 0.19 wt.%, while SiO_2 content ranged from 46.36 to 78.56 wt.%. The CaO content in run DO1 was higher than that of the initial silicate, likely due to the reduction and dissolution of anhydrite. Other major elements in the silicate melts closely matched those in the initial silicates. EPMA totals for silicate melts ranged from 98.02 to 99.49 wt.%. The S content in the silicate melt at sulfide saturation (SCSS) ranged from 328 to 3889 μg/g. As shown in Fig. S3, the S content of silicate melts in reduced experiments followed a U-shaped dependence on FeO_{tot} content at a given temperature, with SCSS increasing with temperature. These findings align with previous studies on SCSS (O'Neill and Mavrogenes, 2002; Smythe et al., 2017; Wykes et al., 2015). The silicate melt in run DO1, which included anhydrite, had a S content of 1173 μg/g, significantly higher than the 328 μg/g measured in run ED-2, which was conducted at similar temperature, pressure, and silicate composition. This indicates a higher fO_2 in run DO1. Trace elements Cu, Ni, Se, and Te were homogeneously distributed in the silicate melts, with concentrations ranging from 7 to 165 μg/g for Cu, 2–161 μg/g for Ni, 2–20 μg/g for Se, and 0.3–27 μg/g for Te.

The Fe–Ni–Cu–S sulfide liquids contained 28.38–38.94 wt.% S, 38.79–55.91 wt.% Fe, 5.94–14.7 wt.% Ni, 0.93–9.92 wt.% Cu, and 0.43–4.28 wt.% O. Se and Te were homogeneously distributed in the sulfide liquids, with concentrations ranging from 2000 to 17,000 μg/g for Se and 3000–66,000 μg/g for Te. Measurements of Se and Te concentrations in sulfide liquids by EPMA and LA–ICP–MS show strong consistency (Fig. S4).

3.2. Sulfide liquid–silicate melt partitioning of Se and Te

We calculated $D_{Se,\ Te,\ S,\ Cu}^{Sul/Sil}$ using the weight proportions of Se, Te, S, and Cu in sulfide liquid and silicate melt (Tables S2 and S3). The results indicate that $D_{Se}^{Sul/Sil}$ range between 180 and 2200, $D_{Te}^{Sul/Sil}$ between 1000 and 25,400, $D_{S}^{Sul/Sil}$ between 80 and 1000, and $D_{Cu}^{Sul/Sil}$ between 260 and 4200 (Table 1). Temperature has an unresolved effect on $D_{Se,\ Te}^{Sul/Sil}$ (Fig. 1a and b), but $D_{S,\ Cu}^{Sul/Sil}$ decrease with increasing temperature (Fig. S5A and B). $D_{Se,\ Te}^{Sul/Sil}$ exhibit an inverted U-shaped dependence on the FeO_{tot} content in silicate melt (Fig. 1c and d), similar to $D_{S}^{Sul/Sil}$ (Fig. S5C). This inverted U-shaped dependence aligns with the U-shaped FeO_{tot}-dependence of the S or Se content in silicate melt at sulfide or selenide saturation (Fig. S3A) (Smythe et al., 2017; Wykes et al., 2015). The underlying explanation for such U-shaped FeO_{tot}-dependence is the trade-off between the positive effect of FeO_{tot} and the negative effect of the FeO_{tot} activity on the S or Se content in silicate melt (Smythe et al., 2017; Wykes et al., 2015). Our $D_{Se,\ Te}^{Sul/Sil}$ show no dependence on the Ni content of sulfide liquid (Fig. 2). $D_{Cu}^{Sul/Sil}$ are larger than $D_{Se}^{Sul/Sil}$ but smaller than $D_{Te}^{Sul/Sil}$, and the $D_{Se}^{Sul/Sil}/D_{Te}^{Sul/Sil}$ ratios are smaller than 0.4 (Fig. 3). Our $D_{Cu}^{Sul/Sil}$ are well consistent with the results predicted using a previous partitioning model (Li et al., 2021) (Fig. S6).

Previous $D_{Se,\ Te}^{Sul/Sil}$ obtained for reduced lunar basalts (fO_2 = ~FMQ-5) (Steenstra et al., 2018) and oxidized arc magmas (fO_2 = ~FMQ+1.5) (Li et al., 2021) are systematically consistent with our new $D_{Se,\ Te}^{Sul/Sil}$ (Fig. 1c and d), indicating a negligible effect of fO_2 on $D_{Se,\ Te}^{Sul/Sil}$ in the presently studied range of fO_2. It is likely that at $fO_2 \leq$ FMQ+1.5, both Se and Te exist in a valence state of 2- in silicate melt (Jenner et al., 2010), whereas S predominantly exists as S^{6+} at $fO_2 \geq$ FMQ+1 (Jugo et al., 2010). This agrees with previous knowledge that the transition from selenide and telluride to oxyanions requires higher fO_2 compared to sulfide (Brookins, 1988; Renggli et al., 2022). Fig. 1c and D also shows that our new $D_{Se,\ Te}^{Sul/Sil}$ are consistent with the partitioning data derived from

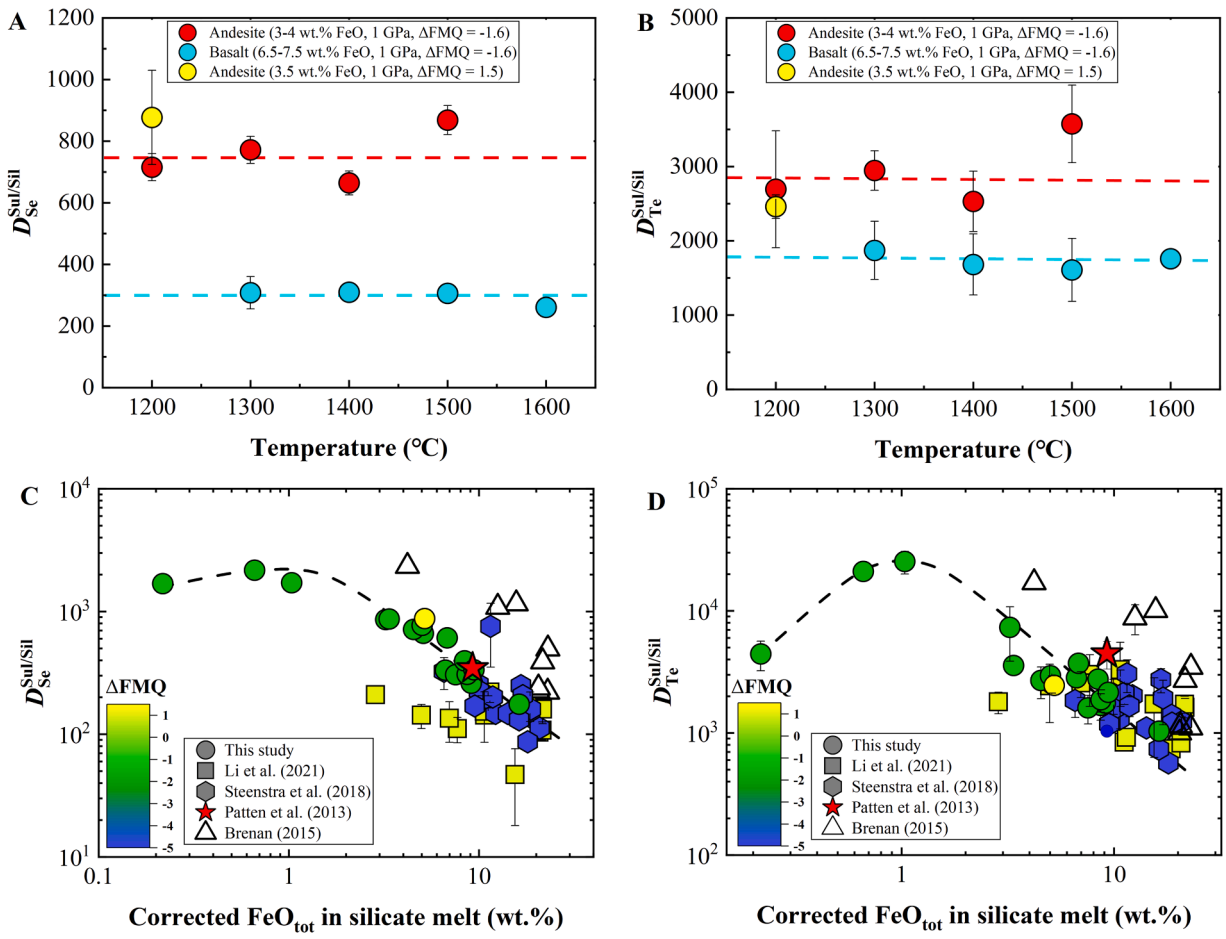

Fig. 1. Sulfide liquid–silicate melt partition coefficients of Se and Te ($D^{Sul/Sil}_{Se,\ Te}$). (A, B) The plot of $D^{Sul/Sil}_{Se,\ Te}$ from the experiments on basaltic and andesitic melts as a function of temperature, showing a negligible effect of temperature on $D^{Sul/Sil}_{Se,\ Te}$. (C, D) The plot of $D^{Sul/Sil}_{Se,\ Te}$ from all experiments as a function of the FeO_{tot} content in silicate melt, corrected for an ideal activity of FeS in sulfide liquid (see the main text). Previous data (Brenan, 2015; Li et al., 2021; Patten et al., 2013; Steenstra et al., 2018) obtained at various conditions or derived from coexisting sulfide liquid and silicate melt in MORBs were plotted for comparison. $D^{Sul/Sil}_{Se,\ Te}$ initially increase but then decrease with decreasing the FeO_{tot} content in silicate melt; however, $D^{Sul/Sil}_{Se,\ Te}$ do not show an fO_2-dependence in the experimental fO_2 range of FMQ-5 to FMQ+1.5.

coexisting sulfide liquid and silicate melt in MORBs (Patten et al., 2013). Our $D^{Sul/Sil}_{Se,\ Te}$ cannot be directly compared to the unpublished $D^{Sul/Sil}_{Se,\ Te}$ values reported in Kiseeva et al. (2017) due to the lack of their experimental details. However, the $D^{Sul/Sil}_{Se,\ Te}$ data from Brenan (2015) are significantly higher than others (Fig. 1c and d). This discrepancy cannot be attributed to the difference in Cu and Ni content of the sulfide liquids (Fig. 2). Future experiments are needed to investigate the underlying causes of this discrepancy. The unusually high $D^{Sul/Sil}_{Se,\ Te}$ and low $D^{Sul/Sil}_{Cu}/D^{Sul/Sil}_{Se,\ Te}$ ratios (Fig. 3) may explain why the $D^{Sul/Sil}_{Se,\ Te}$ from Brenan (2015) failed to accurately account for the relative behaviors of Se, Te, and Cu in both MORBs and arc magmas (Brenan, 2015; Yierpan et al., 2019).

3.3. Thermodynamics of the sulfide liquid–silicate melt partitioning of Se and Te

Like S, Se and Te could replace O as Se^{2-} and Te^{2-} in silicate melt, which can be described by the following reaction (taking Se as an example):

$$O^{2-} + 1/2Se_2 = Se^{2-} + 1/2O_2 \quad (1)$$

The equilibrium constant K of reaction (1) can be written as:

$$logK_{(1)} = logX^{Sil}_{Se^{2-}} - logX^{Sil}_{O^{2-}} + 1\Big/2\log\left(\frac{fO_2}{fSe_2}\right) \quad (2)$$

where $X^{Sil}_{Se^{2-}}$ and $X^{Sil}_{O^{2-}}$ are the concentration of Se^{2-} and O^{2-} in silicate melt, respectively. Since the number of O atoms in silicate melts greatly exceeds the number of other potential anions, $X^{Sil}_{O^{2-}}$ can be assumed to be constant (O'Neill and Mavrogenes, 2002). Similar to the sulfide capacity (O'Neill and Mavrogenes, 2002), we proposed the selenide capacity C_{Se} as below:

$$logC_{Se} = logX^{Sil}_{Se^{2-}} + 1\Big/2\log\left(\frac{fO_2}{fSe_2}\right) \quad (3)$$

Again similar to the sulfide capacity (O'Neill and Mavrogenes, 2002; Smythe et al., 2017), the selenide capacity C_{Se} can be modeled with respect to the chemical composition of the silicate melt:

$$logC_{Se} = \sum_{1}^{i} c_i * X^{Sil}_i \quad (4)$$

where X^{Sil}_i stands for the mole fraction of an oxide in silicate melt (e.g., FeO, MgO), and c_i is a coefficient.

The partitioning of Se between sulfide liquid and silicate melt can be described by the following reaction:

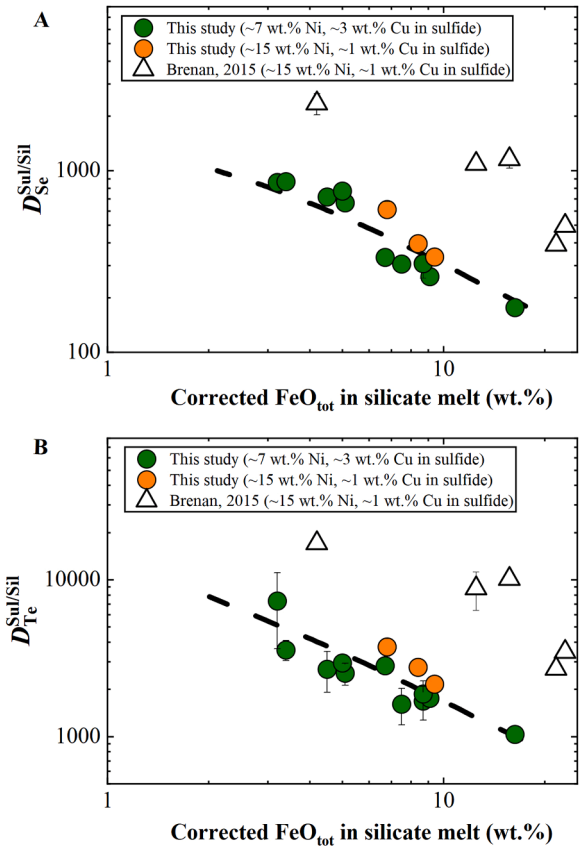

Fig. 2. Sulfide liquid–silicate melt partition coefficients of Se and Te ($D_{Se,\ Te}^{Sul/Sil}$). (A, B) The plot of $D_{Se,\ Te}^{Sul/Sil}$ from the experiments on basaltic, andesitic, and dacitic melts as a function of the FeO_{tot} content in silicate melt, corrected for an ideal activity of FeS in sulfide liquid (see the main text). Previous $D_{Se,\ Te}^{Sul/Sil}$ data from Brenan (2015) are significantly higher than those in this study, although the sulfide liquid compositions in Brenan (2015) are nearly identical to those of some of our sulfide liquids (~15 wt.% Ni and ~1 wt.% Cu). This figure demonstrates that the difference between the present $D_{Se,\ Te}^{Sul/Sil}$ and those of Brenan (2015) cannot be attributed to effect of sulfide liquid composition.

$$FeO_{sil} + 1/2Se_2 = FeSe_{sul} + 1/2O_2 \tag{5}$$

The following equation can be derived from reaction (5):

$$logK_{(5)} = -\frac{\Delta G^0}{(2.303RT)} = loga_{FeSe}^{Sul} - loga_{FeO}^{Sil} + 1\Big/2\log\left(\frac{fO_2}{fSe_2}\right) \tag{6}$$

where $K_{(5)}$ is the equilibrium constant of reaction (5); ΔG^0 is the free energy of reaction (5); T is the temperature in K; R is the ideal gas constant; a_{FeSe}^{Sul} and a_{FeO}^{Sil} are the activity of FeSe in sulfide liquid and FeO in silicate melt, respectively. By combining (3) and (6) we obtained:

$$-\frac{\Delta G^0}{(2.303RT)} = loga_{FeSe}^{Sul} - loga_{FeO}^{Sil} + logC_{Se} - logX_{Se^{2-}}^{Sil} \tag{7}$$

The activity of FeSe in sulfide liquid and FeO in silicate melt can be expressed as follows:

$$a_{FeSe}^{Sul} = X_{FeSe}^{Sul} * \gamma_{FeSe}^{Sul} \tag{8}$$

$$a_{Feo}^{Sil} = X_{Feo}^{Sil} * \gamma_{Feo}^{Sil} \tag{9}$$

where γ_{FeSe}^{Sul} and X_{FeSe}^{Sul} are the activity coefficient and mole fraction of FeSe in sulfide liquid, respectively; γ_{FeO}^{Sil} and X_{FeO}^{Sil} are the activity coefficient and mole fraction of FeO in silicate melt, respectively. Thus, the partition coefficients of Se between sulfide liquid and silicate melt can be written as:

$$logD_{Se}^{Sul/Sil} = logX_{FeO}^{Sil} + log\gamma_{FeO}^{Sil} - logC_{Se} - log\gamma_{FeSe}^{Sul} - \frac{\Delta G^0}{(2.303RT)} + C \tag{10}$$

where C is a constant. The silicate melt composition may influence γ_{FeO}^{Sil} and C_{Se} (O'Neill and Mavrogenes, 2002; Smythe et al., 2017), and the sulfide liquid composition may influence γ_{FeSe}^{Sul} (Boujibar et al., 2014; Kiseeva and Wood, 2015; Smythe et al., 2017). We used the following approximations:

$$log\gamma_{FeO}^{Sil} - logC_{Se} \approx \sum_{1}^{i} d_i * X_i^{Sil} \tag{11}$$

$$log\gamma_{FeSe}^{Sul} \approx \frac{1273}{T}\sum_{1}^{i} e_i * log\left(1 - X_i^{Sul}\right) \tag{12}$$

where d_i is a coefficient that describes the effect of an oxide on $D_{Se}^{Sul/Sil}$; X_i^{Sul} is the mole fraction of FeS, NiS, Cu_2S, or FeO in sulfide liquid; and e_i is a coefficient that describes the non-ideal interaction between Se and sulfide matrix. We then obtained the following equation to describe $D_{Se}^{Sul/Sil}$:

$$logD_{Se,\ Te}^{Sul/Sil} = log\left(X_{FeO_{tot}}^{Sil}\right)_{corr} + \frac{a}{T} + b * \frac{P}{T} + \sum_{1}^{i} d_i * X_i^{Sil} + \frac{1273}{T}\sum_{1}^{i} e_i * log\left(1 - X_i^{Sul}\right) + C \tag{13}$$

where P is pressure in GPa; a and b are coefficients. In Eq. (13), for simplification and following previous studies (Kiseeva and Wood, 2015; Li et al., 2021), we treated the total Fe oxides in silicate melt as FeO $\left(X_{FeO_{tot}}^{Sil}\right)$, without considering the Fe^{3+} fraction within the fO_2 range of sulfide stability. In addition, we corrected the mole fraction of total Fe oxides in silicate melt $\left(X_{FeO_{tot}}^{Sil}\right)_{corr}$ to reflect the ideal activity of FeS in sulfide liquid as follows:

$$\left(X_{FeO}^{Sil}\right)_{corr} = \left(X_{FeO}^{Sil}\right)\Big/\left[\left(X_{Fe}^{Sul}\Big/\left(X_{Fe}^{Sul} + X_{Ni}^{Sul} + X_{Cu}^{Sul}\right]\right.\right. \tag{14}$$

Excluding the $D_{Se,\ Te}^{Sul/Sil}$ data from Brenan (2015), we fitted the $D_{Se,\ Te}^{Sul/Sil}$ values from this study and previous studies (Li et al., 2021; Steenstra et al., 2018) into Eq. (13). The used $D_{Se,\ Te}^{Sul/Sil}$ data were obtained at pressures of 0.5–2.5 GPa, temperatures of 1273–1973 K, and fO_2 of ~FMQ-5 to FMQ+1.5; the silicate melts contained 0.2–21 wt.% FeO_{tot}; and the sulfide liquids contained 0–45 wt.% Cu, 0–15 wt.% Ni, and up to 5 wt.% O. Using multiple linear regression, we derived the following equations to best describe $D_{Se,\ Te}^{Sul/Sil}$:

$$\begin{aligned} logD_{Se}^{Sul/Sil} = {} & log\left(X_{FeO_{tot}}^{Sil}\right)_{corr} - 6.89\ (1.29)\cdot\left(X_{FeO}^{Sil}\right)_{corr} - 3.1\ (1.03)\cdot X_{MgO}^{Sil} \\ & - 15.28\ (4.64)\cdot X_{Na_2O}^{Sil} - 5.97(1.50)\cdot X_{CaO}^{Sil} - 5.52(1.59)\cdot X_{TiO_2}^{Sil} \\ & + \frac{1273}{T}\cdot 1.50\ (0.47)\cdot\log\left(1 - X_{CuS_{0.5}}^{Sul}\right) \\ & + 5.77\ (0.23)\ \left(R^2 = 0.86;\ N = 48;\ 2\sigma = 0.5\right) \end{aligned} \tag{15}$$

$$\begin{aligned} logD_{Te}^{Sul/Sil} = {} & log\left(X_{FeO_{tot}}^{Sil}\right)_{corr} - 5.94\ (0.81)\cdot\left(X_{FeO}^{Sil}\right)_{corr} - 9.29\ (2.16)\cdot X_{Na_2O}^{Sil} \\ & + 57.55\ (5.83)\cdot X_{K_2O}^{Sil} \\ & + 4.91\ (0.11)\ \left(R^2 = 0.90;\ N = 48;\ 2\sigma = 0.44\right) \end{aligned} \tag{16}$$

Eqs. (15) and (16) imply that the composition of the silicate melt, particularly the FeO_{tot} content, has a significant effect on $D_{Se,\ Te}^{Sul/Sil}$, while the composition of the sulfide liquid has a lesser influence. Moreover,

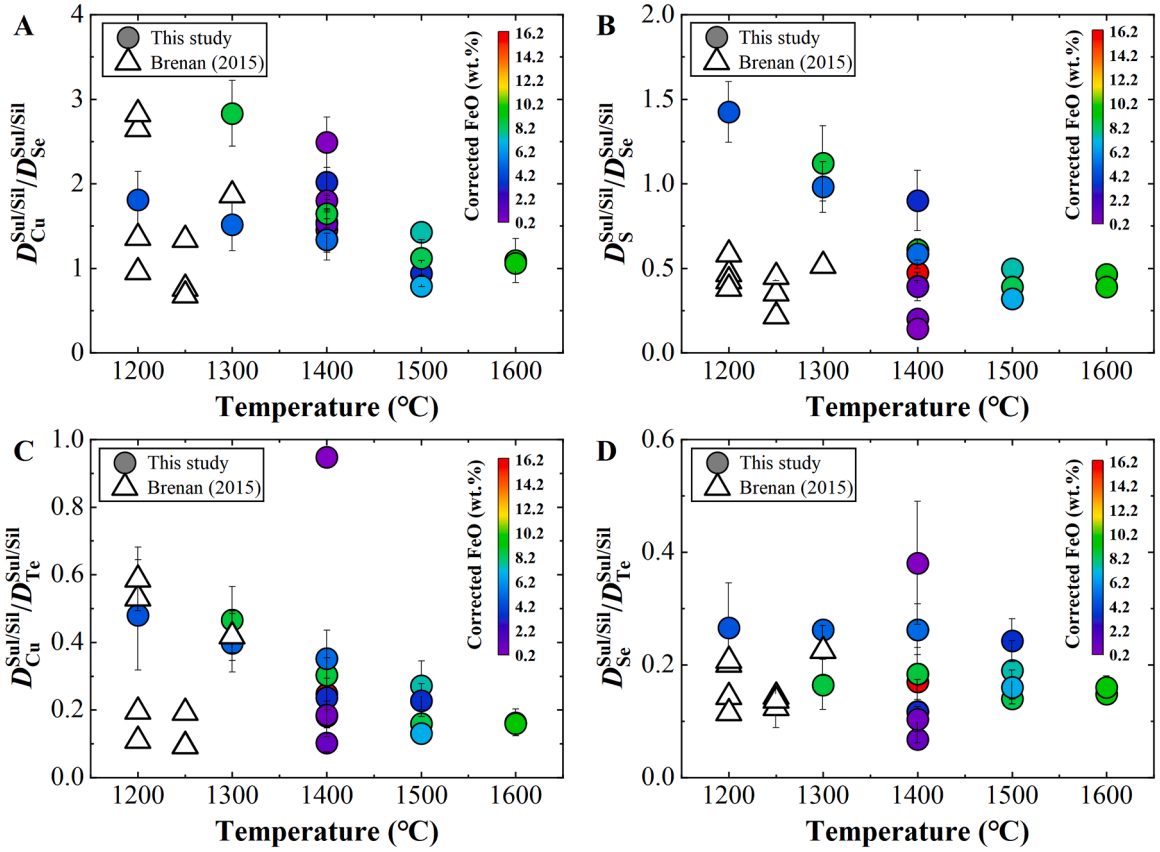

Fig. 3. The ratios of sulfide liquid–silicate melt partition coefficients of Cu, S, Se, and Te ($D_{Cu}^{Sul/Sil}/D_{Se}^{Sul/Sil}$, $D_{S}^{Sul/Sil}/D_{Se}^{Sul/Sil}$, $D_{Cu}^{Sul/Sil}/D_{Te}^{Sul/Sil}$, and $D_{Se}^{Sul/Sil}/D_{Te}^{Sul/Sil}$) as a function of temperature. (A-D) The $D_{Cu}^{Sul/Sil}/D_{Se}^{Sul/Sil}$, $D_{S}^{Sul/Sil}/D_{Se}^{Sul/Sil}$, and $D_{Cu}^{Sul/Sil}/D_{Te}^{Sul/Sil}$ ratios all increase with decreasing temperature, while the $D_{Se}^{Sul/Sil}/D_{Te}^{Sul/Sil}$ ratios are nearly constant. The data of Brenan (2015) were plotted for comparison, and the $D_{Cu}^{Sul/Sil}/D_{Se}^{Sul/Sil}$, $D_{S}^{Sul/Sil}/D_{Se}^{Sul/Sil}$, and $D_{Cu}^{Sul/Sil}/D_{Te}^{Sul/Sil}$ ratios are generally lower than those determined in this study.

our trial-and-error fitting demonstrated that none of the parameters—such as pressure (0.5–2.5 GPa), temperature (1273–1973 K), fO_2 (ΔFMQ = −5–1.5), or the concentrations of Se and Te in the sulfide liquid—exert a considerable effect on $D_{Se,\ Te}^{Sul/Sil}$.

4. Discussion

4.1. Model Se and Te behavior during magmatic differentiation

We investigated whether our $D_{Se,\ Te}^{Sul/Sil}$, along with $D_{Cu}^{Sul/Sil}$ (Li et al., 2021), can explain the Se, Te, and Cu systematics observed in differentiated MORBs and oxidized arc magmas. We used the Se, Te, and Cu systematics of MORBs from Pacific–Antarctic ridge (Yierpan et al., 2019), and the Se and Cu systematics of oxidized back arc magmas from Eastern Manus Basin and Lau Basin (Jenner et al., 2012, 2010). A fractional crystallization model with the following conditions was used. **(i)** The differentiation pressure was fixed at 0.2 GPa, and major element compositions of the magmas were used to calculate the liquidus temperatures, using the MELTS program (Ghiorso et al., 2002). **(ii)** The mass fraction of residual silicate melt during magmatic differentiation was calculated using a highly incompatible element, such as La or Y. **(iii)** We used the model from a recent study (Smythe et al., 2017) to calculate the S content in silicate melt at sulfide saturation (SCSS), and then we used the change of SCSS at each step of fractional crystallization to determine the mass of segregated sulfides. **(iv)** During MORB differentiation, sulfide liquid was saturated and segregated (Yierpan et al., 2019); while, the segregated sulfides from arc magmas included both sulfide liquid and crystalline monosulfide-solid-solution (MSS) due to the low temperatures (Li et al., 2021). Assuming Fe–Cu–O–S sulfide liquid and Fe–Cu–S MSS in arc magmas, and Fe–Cu–Ni–O–S sulfides in MORBs, we calculated the Cu and Ni content in sulfides using an iterative approach based on the partitioning of Cu and Ni between sulfide and silicate melt (Li et al., 2021). The O content in sulfide liquid was calculated based on the FeO_{tot} content in silicate melt (Kiseeva and Wood, 2013). **(V)** The $D_{Cu}^{Sul/Sil}$ and $D_{Cu}^{MSS/Sil}$ used were calculated using a recent partitioning model (Li et al., 2021), and the $D_{Se,\ Te}^{Sul/Sil}$ used were calculated from our Eqs. (15) and (16). The $D_{Se}^{MSS/Sil}$ used were calculated from $D_{Se}^{Sul/Sil} \cdot D_{Se}^{MSS/Sul}$, using a $D_{Se}^{MSS/Sul}$ value of 0.48 ± 0.05 (N = 5; 1σ) obtained for oxidized arc magmas (Li et al., 2021). We assumed perfect incompatibility of Se, Te, and Cu in silicate and oxide minerals (Brenan, 2015; Li et al., 2022; Yierpan et al., 2019). **(VI)** For the differentiation of oxidized arc magmas, we first modeled the behavior of Cu to constrain the mass ratio of segregated sulfide liquid vs. MSS, and then we used the conditions that can reproduce the Cu systematics to model the behavior of Se.

Full modeling conditions are provided in Table S4. Fig. 4A and Fig. S7A illustrate that the abrupt drop in Cu from 280 to 40 μg/g and Se from 0.37 to 0.2 μg/g in the lavas from Manus Basin (Jenner et al., 2010) can be attributed to the fractionation of sulfide liquid, followed by the co-fractionation of MSS and sulfide liquid. Ultimately, the fractionation of MSS is responsible for the gradual decline in Cu content and the slight increase in Se content when the magmas contained < 30 μg/g Cu and < 0.2 μg/g Se. The determined mass ratio of MSS to sulfide liquid during their co-fractionation is about 1: 2. In the case of the lavas from Lau Basin (Jenner et al., 2012), the Cu content decreases as the MgO content decreases after sulfide saturation and segregation (Fig. S7B), while the

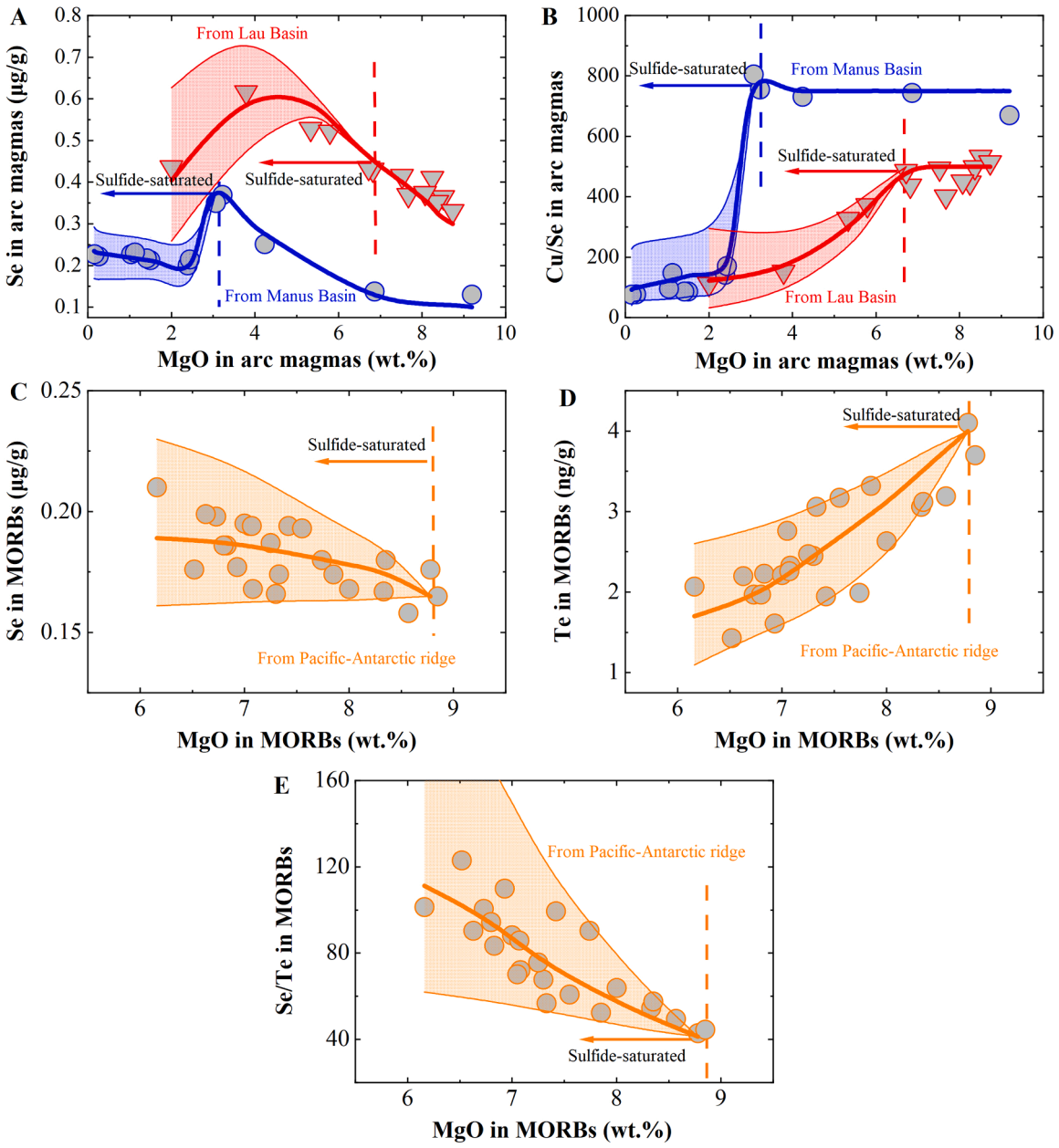

Fig. 4. Comparison of the modeled Se, Te contents and Cu/Se, Se/Te ratios with the observed values in arc magmas and MORBs. (A, B) The modeled vs. observed Se and Cu/Se systematics as a function of the MgO content in back arc magmas from Manus Basin (Jenner et al., 2010) and Lau Basin (Jenner et al., 2012). (C, D, E) The modeled vs. observed Se, Te, and Se/Te systematics as a function of the MgO content in MORBs from Pacific–Antarctic ridge (Yierpan et al., 2019). The colored areas represent the modeled results that consider the errors of $D^{Sul/Sil}_{Se,\ Te}$ calculated from Eqs. (15) and (16). Note that in panels (A–D) the decrease in Se and Te content and Cu/Se ratio in both arc magmas and MORBs is caused by the segregation of sulfides. During MORB differentiation, the segregated sulfides are pure sulfide liquid, whereas during arc magmatic differentiation, the segregated sulfides are sulfide liquid ± MSS; more details are given in Fig. S7. This figure illustrates that our $D^{Sul/Sil}_{Se,\ Te}$, in conjunction with the magmatic differentiation model, can fully explain the Se, Te, and Cu systematics of both oxidized arc magmas and MORBs.

Se content initially increases and then decreases with decreasing MgO content (Fig. 4a). This behavior can be attributed to an insufficient mass of segregated sulfide liquid to lower the Se content until the fractionation of magnetite triggers the fractionation of more sulfides at ~4 wt.% MgO (Jenner et al., 2012). The fractionated sulfide phases change from being solely sulfide liquid to coexisting MSS and sulfide liquid, with a determined mass ratio of about 1: 2. Furthermore, our modeled Cu/Se ratios are consistent with the observed data (Fig. 4b). Fig. 4b shows that the Cu/Se ratios remain nearly constant prior to sulfide saturation, but then decrease with decreasing MgO content after sulfide saturation. This suggests that Cu is more compatible than Se in sulfides. In the context of MORB differentiation, Fig. 4c and Fig. 4d demonstrate that the fractionation of sulfide liquid can account for the increase in Se and the decrease in Te with decreasing MgO content. The observed Se/Te ratios in MORBs can also be explained, and the increase in Se/Te ratio with decreasing MgO content (Fig. 4e) indicates, and further confirms, that Te is more compatible than Se in the sulfide liquid during MORB differentiation (Lissner et al., 2014; Yierpan et al., 2019). The success of our $D^{Sul/Sil}_{Se,\ Te}$ in explaining the observed Se, Te, and Cu systematics of both MORBs and oxidized arc magmas underscores the reliability and validity of our Eqs. (15) and (16) when applied to crust–mantle magmatic processes.

4.2. Model Se and Te behavior during mantle melting and Se And Te abundances in the silicate Earth

As a further step, we used Eqs. (15) and (16) to model the behavior of Se and Te during mantle melting. By combining this with the calculated Se and Te contents of primary MORBs from the Pacific–Antarctic ridge (Yierpan et al., 2019), we can estimate the abundances of Se and Te in the DMM using the same approach as Yierpan et al. (2019). The primary MORBs from Pacific–Antarctic ridge were produced by a mean mantle melting degree of 8.5 ± 1.5 % (Yierpan et al., 2019). To model the behavior of Se and Te during mantle melting, we used a triangular passive-flow near-fractional decompression melting model (Plank and Langmuir, 1992; Rehkämper et al., 1999), similar to previous studies that modeled PGEs and Se and Te (Brenan, 2015; Mungall and Brenan, 2014; Yierpan et al., 2019). In this model, the maximum degree of melting (F_{max}) is only achieved in a central column, with reduced melting in surrounding regions. Therefore, the Se and Te concentrations in the aggregate melt produced in a columnar melting regime were first calculated. The Se and Te concentrations of each melting increment (1.1 %) were calculated by using the batch melting equation. After each melting increment, 10 % of the melt is retained to refertilize the residual mantle column, and the rest (90 %) is extracted. The compositions of the mantle residue are recalculated as the source for the next melting step. The polybaric column-melts produced over the entire melting zone are pooled, and the mean extent of melting (F_{mean}) is defined as $F_{max}/2$ (Plank and Langmuir, 1992). The Se and Te concentrations of an aggregate melt produced in a triangular melting regime can be calculated from the average of all the pooled melts (Rehkämper et al., 1999).

Major element composition of the DMM (Workman and Hart, 2005) was used as the mantle composition before melting, with Fe_2O_3 content assumed to be 0.20 wt.% (Cottrell and Kelley, 2011). The depth of first melting (~1.7 GPa) was constrained based on the nominally volatile-free peridotite solidus, and the mantle potential temperature was 1350 °C. As the degree of melting increases from 0 to 30 %, the pressure decreases from ~1.7 to 0.2 GPa, and the temperature decreases from ~1400 to 1289 °C. Details of such an isentropic decompression melting model were given in previous studies (Ding and Dasgupta, 2017; Li et al., 2022; Yierpan et al., 2019). Major elements compositions of mantle melt in a melting column were calculated using pMELTS (Ghiorso et al., 2002). As the degree of melting increases from 0 to 30 %, the FeO_{tot} content of partial melts decreases from ~10.4 to 6.4 wt.%, and the MgO content decreases from 14.9 to 11.9 wt.%. The SCSS in partial melts was calculated using the model of Smythe et al. (2017). The mantle was assumed to contain 150–250 μg/g S as sulfide liquid during partial melting (Wang and Becker, 2015a; Zhang and Hirschmann, 2016), and the sulfide liquid has 38 wt.% S, 25 wt.% Ni, and 5 wt.% Cu (Ding and Dasgupta, 2017). Se and Te were assumed to be completely incompatible in mantle minerals, and the applied $D^{Sul/Sil}_{Se,\ Te}$ were calculated using Eqs. (15) and (16). The modeling program with detailed parameters is provided in Table S5.

Fig. 5 illustrates that the modeled Se contents in MORBs decrease with increasing melting degree (F_{mean}), while the modeled Te contents increase with increasing F_{mean}. Furthermore, the modeled Se/Te ratios in MORBs decrease as F_{mean} increases, which reflects the higher compatibility of Te than Se during mantle melting. Our model yielded 20 ± 5 ng/g Se and 1.35 ± 0.7 ng/g Te in the DMM to effectively explain

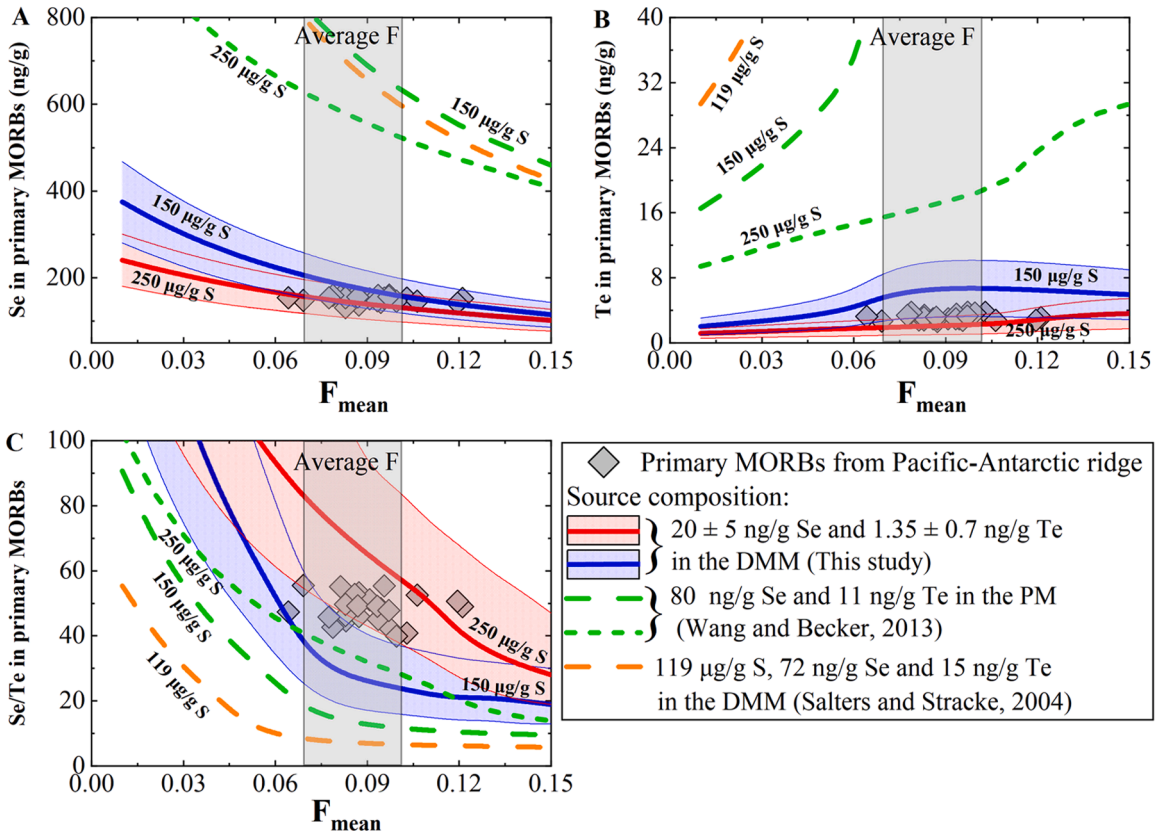

Fig. 5. The modeled Se–Te contents and Se/Te ratios in primary MORBs as a function of the degree of mantle partial melting (F_{mean}). (A–C) The calculated Se–Te contents and Se/Te ratios in primary MORBs from Pacific–Antarctic ridge are plotted. These primary melt Se–Te contents are corrected from the differentiated MORBs (Yierpan et al., 2019) after calculating crystal and sulfide fractionation using our new $D^{Sul/Sil}_{Se,\ Te}$. The colored areas represent the modeled results, using 20 ± 5 ng/g Se, 1.35 ± 0.7 ng/g Te, and 150–250 μg/g S in the depleted MORB mantle (DMM), which can reproduce the observed Se and Te contents and Se/Te ratios in the primary MORBs. The green and yellow lines represent the modeled results using Se and Te abundances given by Wang and Becker (2013) for the PM and by Salters and Stracke (2004) for the DMM, which, however, cannot match the observations.

the Se and Te contents and Se/Te ratios in the primary MORBs from the Pacific–Antarctic ridge (Yierpan et al., 2019). These values are lower than the estimates for the DMM by Salters and Stracke (2004) (72 ng/g Se and 15 ng/g Te) and by Yierpan et al. (2019) (49 ± 11 to 80 ± 17 ng/g Se; 3.5 ± 1.3 to 11 ± 1.7 ng/g Te).

Furthermore, we can estimate the Se and Te abundances in the PM by assuming that the DMM represents the residuals of the PM after extracting ~2–3 % melt (Salters and Stracke, 2004; Workman and Hart, 2005; Yierpan et al., 2019). For partial melting of the PM to generate the DMM, we used a S content of 250 μg/g in the PM (McDonough and Sun, 1995), 1200 μg/g of S in the generated melt at sulfide saturation, a $D_{Se}^{Sul/Sil}$ value of 150, and a $D_{Te}^{Sul/Sil}$ value of 1200. We also assumed perfect incompatibility of Se and Te in mantle silicate and oxide minerals. Using our estimated abundances of 20 ± 5 ng/g Se and 1.35 ± 0.7 ng/g Te in the DMM, we obtained 25 ± 5 ng/g Se and 1.37 ± 0.7 ng/g Te in the PM. These values are nearly identical to the Se and Te abundances in the DMM due to the high $D_{Se,\ Te}^{Sul/Sil}$ and the limited degree of melting. Moreover, these values are lower than the estimates for the PM by McDonough and Sun (1995) (75 ± 20 ng/g Se; 12 ± 3 ng/g Te), Wang and Becker (2013) (80 ± 17 ng/g Se; 11 ± 1.7 ng/g Te), and Yierpan et al. (2019) (49 ± 11 to 80 ± 17 ng/g Se; 3.5 ± 1.3 to 11 ± 1.7 ng/g Te).

As illustrated in Fig. 5, if we apply the Se and Te abundances in the DMM and in the PM estimated by Salters and Stracke (2004) and Wang and Becker (2013), respectively, the modeled Se and Te contents significantly exceed the observed values for the primary MORBs. This demonstrates that early studies may have overestimated the Se and Te abundances in the DMM and the PM.

4.3. The discrepancy in the estimated Se and Te abundances in the silicate Earth

Our estimated Se and Te abundances in the PM are lower than previous estimates (Fig. 6). We propose possible reasons for these discrepancies. First, we note that the DMM may contain some pyroxenites, formed through reactions between the melts derived from recycled oceanic crust and the ambient mantle peridotite (Sobolev et al., 2007). If the melt proportion is 5 % compared to the ambient mantle peridotite and 10–15 % of MORB melts are contributed by pyroxenite-derived melts (Sobolev et al., 2007), we calculate that Se and Te abundances in the DMM should not exceed our estimates by 15 %, assuming that pyroxenite-derived melts are free of Se and Te. Conversely, if MORBs' Se and Te contents are mainly sourced from pyroxenite-derived melts, then Se and Te abundances in the DMM without containing pyroxenites would be even lower than our estimates. Thus, the presence of a portion of pyroxenites in the DMM does not significantly influence our estimated Se and Te abundances, nor our conclusion that Se and Te abundances in both the DMM and PM are lower than previous estimates. Second, since we used the same Se and Te datasets of MORBs and mantle melting model as Yierpan et al. (2019), the difference between our estimated abundances and those in Yierpan et al. (2019) is mainly due to the lower experimentally determined $D_{Se,\ Te}^{Sul/Sil}$ used in this study, compared to those used by Yierpan et al. (2019) from Brenan (2015). Third, Salters and Stracke (2004) estimated Se and Te abundances in the DMM by assuming that the DMM has Se/V and Te/Ni ratios identical to those of the PM (McDonough and Sun, 1995). Their approach could be flawed because Se, Te, V, and Ni have different behaviors during magmatic genesis and differentiation, and because the Se and Te estimates of McDonough and Sun (1995) may not represent the true PM composition (see below). This may explain the higher Se and Te estimates of Salters and Stracke (2004) than ours.

The high Se and Te abundances in the silicate Earth, estimated by McDonough and Sun (1995) and Wang and Becker (2013), were based on lithospheric mantle lherzolites. In Fig. 7, we show that the Te concentrations and Se/Te ratios in lherzolites cannot be explained by melt extraction alone, regardless of using our estimated Se and Te abundances or those of McDonough and Sun (1995) and Wang and Becker

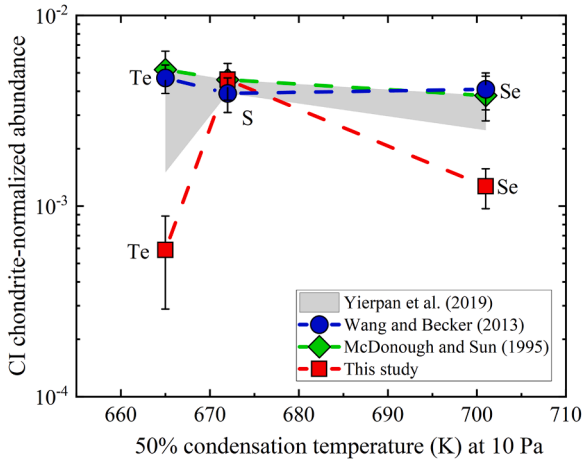

Fig. 6. A plot of the abundances of S, Se, and Te in the primitive mantle (PM) vs. their 50 % condensation temperature at 10 Pa. The 50 % condensation temperature of these elements were taken from Wood et al. (2019). The red squares represent the Se and Te estimates in the PM from this study, and the others were taken from the literature (McDonough and Sun, 1995; Wang and Becker, 2013; Yierpan et al., 2019). Our Se and Te abundances for the PM are lower than previous estimates.

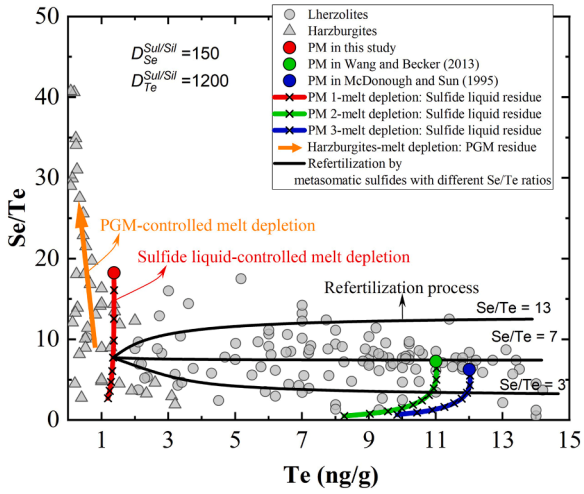

Fig. 7. Se/Te vs. Te for calculated residual and metasomatic solid compositions in comparison with mantle peridotites. The lherzolites and harzburgites data are taken from references (Harvey et al., 2015; König et al., 2015a, 2014, 2012; Lorand and Alard, 2010; Luguet et al., 2015; Morgan, 1986; Wang and Becker, 2013; Wang et al., 2013). The PM compositions of this study, Wang and Becker (2013), and McDonough and Sun (1995) are used as the initial Se and Te contents. We used our new $D_{Se,\ Te}^{Sul/Sil}$ to calculate Se and Te contents in the residual mantle after melt extraction, as shown by the red, green and blue lines, in which each tick mark represents 2 % melt depletion. The modeling results demonstrate that the Se and Te pattern in mantle peridotites cannot be explained by melting depletion involving the fractionation of sulfide liquid, which is the predominant sulfide phase during mantle melting (Jenner et al., 2010; Wang and Becker, 2015a; Zhang and Hirschmann, 2016). The black lines represent the calculated metasomatic solid compositions using simple two component mixing model (depleted harzburgite + metasomatic sulfides with Se/Te ratios of 13, 7, and 3) (König et al., 2014). The Se and Te contents of the metasomatic sulfides are referred to König et al. (2014) (Se and Te: 113 and 9 ng/g; 111 and 15 ng/g, 107 and 38 ng/g). The refertilization model can reproduce the Se and Te pattern in most of the lherzolites. The orange line represents the possible melt depletion signature of harzburgites involving the fractionation of platinum-group minerals (König et al., 2015a).

(2013). Fig. 7 illustrates that, due to $D_{Te}^{Sul/Sil} > D_{Se}^{Sul/Sil}$, the Se/Te ratios in lherzolites decrease sharply with the degree of melting. However, mantle lherzolites display a limited range of Se/Te ratios over a wide range of Te concentrations. These observations support the idea that secondary petrogenetic processes, such as metasomatism, play a crucial role in establishing the observed Se and Te concentrations and Se/Te ratios in lherzolites (Harvey et al., 2015; König et al., 2014; Luguet et al., 2015; Yierpan et al., 2019). Further, Fig. 7 shows that the refertilization model during metasomatism, proposed by König et al. (2014), can explain most lherzolites Se and Te data. In this model, a small proportion (< 15 %) of metasomatic sulfides with different Se/Te ratios, relative to the residual sulfides, is key to determining the Se and Te ranges and ratios observed in lherzolites. It has been observed that mantle lherzolites frequently undergo secondary metasomatism, with metasomatic sulfides common in these rocks (Harvey et al., 2015; König et al., 2015a, 2014; Lorand and Alard, 2010; Luguet et al., 2015). Consequently, Se and Te abundances in the PM, as estimated from lherzolites (McDonough and Sun, 1995; Wang and Becker, 2013), may not represent the true composition of the silicate Earth.

To further verify the reliability of our estimated Se and Te abundances in the DMM and PM, we used these estimates to model Se and Te concentrations in other mantle-derived melts, including primitive arc basalts and MORBs from various locations. Se and Te data from MORBs affected by recycled sediment or oceanic crust were excluded, and a simple batch melting model was applied. Fig. 8 and Fig. S8 illustrate that our estimated Se and Te abundances for the silicate Earth align well with observed Se, Te, and Cu concentrations and ratios in MORBs from southern and northern Mid-Atlantic Ridge (Lissner et al., 2014; Yierpan et al., 2020) and in Mariana arc basalts (Kurzawa et al., 2019). In contrast, the Se, Te, and Cu systematics of most mantle-derived melts are not well explained by previous Se and Te estimates (McDonough and Sun, 1995; Wang and Becker, 2013). These findings indicate that Se and Te systematics differ between the DMM and the lithospheric mantle peridotites, especially when considering the lherzolites' refertilization with metasomatic sulfides. We suggest that our Se and Te estimates for the DMM and PM, based on MORB data, may more accurately reflect the silicate Earth's composition.

4.4. Superchondritic S/Se and S/Te ratios in the silicate Earth

We used 150 ± 50 μg/g S and 250 ± 50 μg/g S in the DMM and PM, respectively, to calculate S/Se, S/Te, and Se/Te ratios for these reservoirs. In Fig. 9, we compared our calculated ratios with previous estimates (McDonough and Sun, 1995; Wang and Becker, 2013; Yierpan et al., 2019) and with chondritic values (Braukmuller et al., 2019; Braukmüller et al., 2018; Dreibus et al., 1995; Friedrich et al., 2003; Wang and Becker, 2013). Our S/Se and S/Te ratios are significantly higher than those in all types of chondrites and previous DMM and PM estimates (Fig. 9a and b). Our Se/Te ratios for the DMM and PM are comparable to those in enstatite chondrites but exceed those in carbonaceous chondrites (CI-, CM-, CV-, and CO-types) (Fig. 9c). The superchondritic S/Se, S/Te, and Se/Te ratios in the DMM and PM relative to carbonaceous chondrites—and the superchondritic S/Se and S/Te ratios relative to both enstatite and carbonaceous chondrites—suggest that the late veneer was not a major source of S, Se, and Te in the silicate Earth. Therefore, Earth's primary accretion likely established these S, Se, and Te systematics.

While our estimated Se/Te ratio for the silicate Earth overlaps with that observed in enstatite chondrites (Fig. 9c), this does not imply that Se and Te in the silicate Earth originated from enstatite chondrite-like late veneer. This is because the estimated S/Se and S/Te ratios for the silicate Earth are superchondritic compared to both enstatite and carbonaceous chondrites. Additionally, the metal–silicate melt partition coefficients of S, Se, and Te (Rose-Weston et al., 2009), which predicted highly siderophile nature of S, Se, and Te and nearly zero Se and Te abundances in the mantle after core-formation and thus underpinned the late veneer model, were obtained at relatively low pressures and temperatures (< 20 GPa and < 2700 K). However, it has been shown that S becomes less siderophile as pressure and temperature increase, suggesting that the S abundance in the silicate Earth could be accounted for by core–mantle partitioning at the conditions of Earth's deep magma ocean (> 40 GPa) (Boujibar et al., 2014; Suer et al., 2017), highlighting the need for further studies on Se and Te behavior at similar conditions.

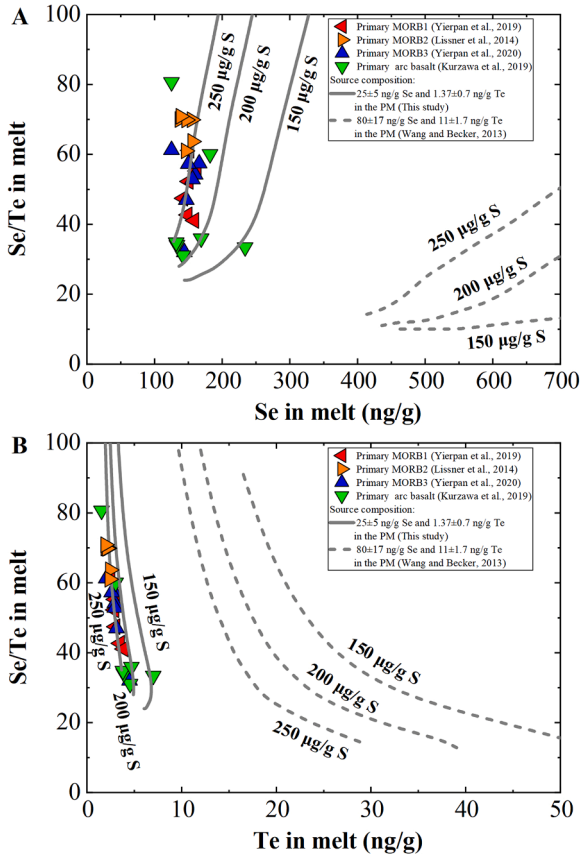

Fig. 8. The modeled Se/Te ratios as a function of Se and Te contents in primary mantle melts. (A, B) The Se and Te contents and Se/Te ratios in primary MORBs from Pacific-Antartic ridge (Yierpan et al., 2019), northern and southern Mid-Atlantic ridge (Lissner et al., 2014; Yierpan et al., 2020), and primary arc basalts from Mariana arc (Kurzawa et al., 2019) are plotted. In order to reduce the effect of sulfide liquid segregation on the Se–Te contents, we only selected the samples with MgO ≥ 8 wt.%. The solid lines represent the modeling results using 25 ± 5 ng/g Se, 1.37 ± 0.7 ng/g Te, and 150–250 μg/g S in the primitive mantle (PM), which can reproduce the observed Se and Te contents and Se/Te ratios in most of the primary mantle melts. The dashed lines represent the modeling results using the Se and Te abundances given by Wang and Becker (2013) and 150–250 μg/g S in the PM, which cannot match the observations.

Our inference that Earth's primary accretion established the S, Se, and Te systematics in the silicate Earth aligns with other constraints on the silicate Earth's volatile inventory, particularly the abundances and isotopic compositions of S, H, and N, which indicate delivery of these volatile elements during the main accretion phase (Labidi et al., 2013; Piani et al., 2020; Shi et al., 2022). A recent study also proposed that S, Se, and Te in the silicate Earth were supplied during the main accretion phase by evaporated planetesimals, based on isotopic signatures (Wang et al., 2023). Furthermore, the view that S, Se, and Te were delivered during the main accretion phase is consistent with the proposal that the late veneer may have consisted of differentiated planetesimals (Marchi et al., 2017), which contributed sufficient PGEs but negligible volatile elements to the proto-Earth's mantle.

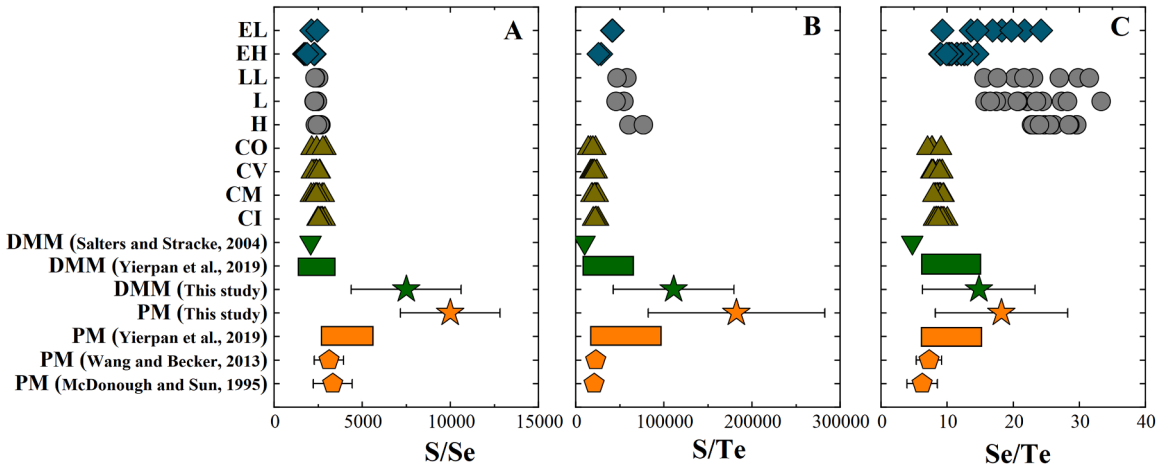

Fig. 9. The S/Se, S/Te, and Se/Te ratios in the depleted MORB mantle (DMM), primitive mantle (PM), and different types of chondrites. Our estimated S/Se (A) and S/Te (B) ratios in the DMM and PM are higher than those in all types of chondrites and previous estimates for the DMM (Salters and Stracke, 2004; Yierpan et al., 2019) and PM (McDonough and Sun, 1995; Wang and Becker, 2013; Yierpan et al., 2019). (C) Our estimated Se/Te ratios in the DMM and PM are higher than those in carbonaceous chondrites (CI-, CM-, CV-, and CO-types) and previous estimates for the DMM (Salters and Stracke, 2004; Yierpan et al., 2019) and PM (McDonough and Sun, 1995; Wang and Becker, 2013), but within the range of estimates of a recent study (Yierpan et al., 2019). The chondrite data taken from references (Braukmuller et al., 2019; Braukmüller et al., 2018; Dreibus et al., 1995; Friedrich et al., 2003; Wang and Becker, 2013).

5. Conclusions

We determined $D^{Sul/Sil}_{Se,\ Te}$ at 1 GPa, 1200–1600 °C, and oxygen fugacity of ~FMQ-1.6 to FMQ+1.5. The $D^{Sul/Sil}_{Se,\ Te}$ values exhibit an inverted U-shaped dependence on the FeO_{tot} content in silicate melt, while temperature and oxygen fugacity have minimal impact. We parameterized $D^{Sul/Sil}_{Se,\ Te}$ as a function of the compositions of both silicate melt and sulfide liquid, enabling us to model the behavior of Se and Te during magmatic differentiation and mantle partial melting. Our model effectively accounts for the Se, Te, and Cu systematics observed in MORBs and oxidized arc magmas. Using high-precision Se and Te data from MORBs collected along the Pacific–Antarctic ridge, we estimated the silicate Earth to contain ~25 ± 5 ng/g of Se and ~1.37 ± 0.7 ng/g of Te. The silicate Earth exhibits superchondritic S/Se and S/Te ratios, suggesting that the late veneer was likely not a major source of S, Se, and Te. Instead, it suggests that the abundances and isotopic compositions of S, Se, and Te in the silicate Earth were established during the main accretion phase. Future experiments should focus on determining the metal–silicate melt partitioning of Se and Te at the conditions of Earth's deep magma ocean. This research will help ascertain whether the current estimates of Se and Te abundances in the silicate Earth can be explained solely by core formation.

CRediT authorship contribution statement

Zhiwei Liu: Writing – review & editing, Writing – original draft, Methodology, Investigation, Formal analysis, Data curation. **Yuan Li:** Writing – review & editing, Writing – original draft, Supervision, Resources, Project administration, Methodology, Investigation, Funding acquisition, Formal analysis, Conceptualization.

Declaration of competing interest

All authors declare that they have no known competing financial interests or personal relationships that could have appeared to influence the work reported in this paper. All authors have read the manuscript and agree to its submission to Earth and Planetary Science letters.

Acknowledgments

We thank James Brenan and two anonymous reviewers for constructive comments. James Badro and Frederic Moynier are thanked for handling this paper.

Supplementary materials

Supplementary material associated with this article can be found, in the online version, at doi:10.1016/j.epsl.2025.119277.

Data availability

All data are available in the main text and the Supplementary Materials.

References

Becker, H., Horan, M.F., Walker, R.J., Gao, S., Lorand, J.P., Rudnick, R.L., 2006. Highly siderophile element composition of the Earth's primitive upper mantle: constraints from new data on peridotite massifs and xenoliths. Geochim. Cosmochim. Acta 70, 4528–4550.
Boujibar, A., Andrault, D., Bouhifd, M.A., Bolfan-Casanova, N., Devidal, J.-L., Trcera, N., 2014. Metal–silicate partitioning of sulphur, new experimental and thermodynamic constraints on planetary accretion. Earth Planet. Sci. Lett. 391, 42–54.
Braukmuller, N., Wombacher, F., Funk, C., Munker, C., 2019. Earth's volatile element depletion pattern inherited from a carbonaceous chondrite-like source. Nat. Geosci. 12, 564–568.
Braukmüller, N., Wombacher, F., Hezel, D.C., Escoube, R., Münker, C., 2018. The chemical composition of carbonaceous chondrites: implications for volatile element depletion, complementarity and alteration. Geochim. Cosmochim. Acta 239, 17–48.
Brenan, J.M., 2015. Se–Te fractionation by sulfide–silicate melt partitioning: implications for the composition of mantle-derived magmas and their melting residues. Earth Planet. Sci. Lett. 422, 45–57.
Brookins, D.G., 1988. Eh-pH Diagrams for Geochemistry. Springer, Berlin Heidelberg.
Cottrell, E., Kelley, K.A., 2011. The oxidation state of Fe in MORB glasses and the oxygen fugacity of the upper mantle. Earth Planet. Sci. Lett. 305, 270–282.
Ding, S., Dasgupta, R., 2017. The fate of sulfide during decompression melting of peridotite – implications for sulfur inventory of the MORB-source depleted upper mantle. Earth Planet. Sci. Lett. 459, 183–195.
Dreibus, G., Palme, H., Spettel, B., Zipfel, J., Wänke, H., 1995. Sulfur and selenium in chondritic meteorites. Meteoritics 30, 439–445.
Fehr, M.A., Hammond, S.J., Parkinson, I.J., 2018. Tellurium stable isotope fractionation in chondritic meteorites and some terrestrial samples. Geochim. Cosmochim. Acta 222, 17–33.
Friedrich, J.M., Wang, M.-S., Lipschutz, M.E., 2003. Chemical studies of L chondrites. V: compositional patterns for 49 trace elements in 14 L4-6 and 7 LL4-6 falls. Geochim. Cosmochim. Acta 67, 2467–2479.

Ghiorso, M.S., Hirschmann, M.M., Reiners, P.W., Victor, C., Kress, I., 2002. The pMELTS: a revision of MELTS for improved calculation of phase relations and major element partitioning related to partial melting of the mantle to 3 GPa. Geochem., Geophys., Geosyst. 3 (5), 1–35.
Harvey, J., König, S., Luguet, A., 2015. The effects of melt depletion and metasomatism on highly siderophile and strongly chalcophile elements: s–Se–Te–Re–PGE systematics of peridotite xenoliths from Kilbourne Hole, New Mexico. Geochim. Cosmochim. Acta 166, 210–233.
Hellmann, J.L., Hopp, T., Burkhardt, C., Becker, H., Fischer-Gödde, M., Kleine, T., 2021. Tellurium isotope cosmochemistry: implications for volatile fractionation in chondrite parent bodies and origin of the late veneer. Geochim. Cosmochim. Acta 309, 313–328.
Jenner, F.E., Arculus, R.J., Mavrogenes, J.A., Dyriw, N.J., Nebel, O., Hauri, E.H., 2012. Chalcophile element systematics in volcanic glasses from the northwestern Lau Basin. Geochem., Geophys., Geosyst. 13, Q06014.
Jenner, F.E., O'Neill, H.S.T.C., Arculus, R.J., Mavrogenes, J.A., 2010. The magnetite crisis in the evolution of arc-related magmas and the initial concentration of Au, Ag and Cu. J. Petrol. 51, 2445–2464.
Jugo, P.J., Wilke, M., Botcharnikov, R.E., 2010. Sulfur K-edge XANES analysis of natural and synthetic basaltic glasses: implications for S speciation and S content as function of oxygen fugacity. Geochim. Cosmochim. Acta 74, 5926–5938.
Kiseeva, E.S., Fonseca, R.O.C., Smythe, D.J., 2017. Chalcophile elements and sulfides in the upper mantle. Elements 13, 111–116.
Kiseeva, E.S., Wood, B.J., 2013. A simple model for chalcophile element partitioning between sulphide and silicate liquids with geochemical applications. Earth Planet. Sci. Lett. 383, 68–81.
Kiseeva, E.S., Wood, B.J., 2015. The effects of composition and temperature on chalcophile and lithophile element partitioning into magmatic sulphides. Earth Planet. Sci. Lett. 424, 280–294.
König, S., Lissner, M., Lorand, J.-P., Bragagni, A., Luguet, A., 2015a. Mineralogical control of selenium, tellurium and highly siderophile elements in the Earth's mantle: evidence from mineral separates of ultra-depleted mantle residues. Chem. Geol. 396, 16–24.
König, S., Lorand, J.-P., Luguet, A., Graham Pearson, D., 2014. A non-primitive origin of near-chondritic S–Se–Te ratios in mantle peridotites; implications for the Earth's late accretionary history. Earth Planet. Sci. Lett. 385, 110–121.
König, S., Luguet, A., Lorand, J.-P., Lissner, M., Graham Pearson, D., 2015b. Reply to the comment on "A non-primitive origin of near-chondritic S–Se–Te ratios in mantle peridotites: implications for the Earth's late accretionary history" by KönigS. Et al. [Earth Planet. Sci. Lett. 385(2014) 110–121]. Earth Planet. Sci. Lett. 417, 167–169.
König, S., Luguet, A., Lorand, J.-P., Wombacher, F., Lissner, M., 2012. Selenium and tellurium systematics of the Earth's mantle from high precision analyses of ultra-depleted orogenic peridotites. Geochim. Cosmochim. Acta 86, 354–366.
Kurzawa, T., König, S., Alt, J.C., Yierpan, A., Schoenberg, R., 2019. The role of subduction recycling on the selenium isotope signature of the mantle: constraints from Mariana arc lavas. Chem. Geol. 513, 239–249.
Labidi, J., Cartigny, P., Moreira, M., 2013. Non-chondritic sulphur isotope composition of the terrestrial mantle. Nature 501, 208–211.
Labidi, J., König, S., Kurzawa, T., Yierpan, A., Schoenberg, R., 2018. The selenium isotopic variations in chondrites are mass-dependent; implications for sulfide formation in the early solar system. Earth Planet. Sci. Lett. 481, 212–222.
Li, Y., Audétat, A., Liu, Z., Wang, F., 2021. Chalcophile element partitioning between Cu-rich sulfide phases and silicate melt and implications for the formation of Earth's continental crust. Geochim. Cosmochim. Acta 302, 61–82.
Li, Y., Li, Y.-X., Xu, Z., 2022. The partitioning of Cu and Ag between minerals and silicate melts during partial melting of planetary silicate mantles. Geochim. Cosmochim. Acta 324, 280–311.
Lissner, M., König, S., Luguet, A., le Roux, P.J., Schuth, S., Heuser, A., le Roex, A.P., 2014. Selenium and tellurium systematics in MORBs from the southern Mid-Atlantic Ridge (47–50°S). Geochim. Cosmochim. Acta 144, 379–402.
Lorand, J.-P., Alard, O., 2010. Determination of selenium and tellurium concentrations in Pyrenean peridotites (Ariege, France): new insight into S/Se/Te systematics of the upper in mantle samples. Chem. Geol. 278, 120–130.
Luguet, A., Behrens, M., Pearson, D.G., König, S., Herwartz, D., 2015. Significance of the whole rock re–Os ages in cryptically and modally metasomatised cratonic peridotites: constraints from HSE–Se–Te systematics. Geochim. Cosmochim. Acta 164, 441–463.
Marchi, S., Canup, R.M., Walker, R.J., 2017. Heterogeneous delivery of silicate and metal to the Earth by large planetesimals. Nat Geosci 11, 77–81.
McDonough, W.F., Sun, S.-s., 1995. The composition of the Earth. Chem. Geol. 120, 223–253.
Médard, E., McCammon, C.A., Barr, J.A., Grove, T.L., 2008. Oxygen fugacity, temperature reproducibility, and H2O contents of nominally anhydrous piston-cylinder experiments using graphite capsules. Am. Mineral. 93, 1838–1844.
Morgan, J.W., 1986. Ultramafic xenoliths: clues to Earth's late accretionary history. J. Geophys. Res. Solid Earth 91, 12375–12387.
Mungall, J.E., Brenan, J.M., 2014. Partitioning of platinum-group elements and Au between sulfide liquid and basalt and the origins of mantle-crust fractionation of the chalcophile elements. Geochim. Cosmochim. Acta 125, 265–289.
O'Neill, H.S.C., Mavrogenes, J.A., 2002. The sulfide capacity and the sulfur content at sulfide saturation of silicate melts at 1400°C and 1 bar. J. Petrol. 43, 1049–1087.
Patten, C., Barnes, S.-J., Mathez, E.A., Jenner, F.E., 2013. Partition coefficients of chalcophile elements between sulfide and silicate melts and the early crystallization history of sulfide liquid: LA-ICP-MS analysis of MORB sulfide droplets. Chem. Geol. 358, 170–188.
Piani, L., Marrocchi, Y., Rigaudier, T., Vacher, L.G., Thomassin, D., Marty, B., 2020. Earth's water may have been inherited from material similar to enstatite chondrite meteorites. Science 369, 1110–1113.
Plank, T., Langmuir, C.H., 1992. Effects of the melting regime on the composition of the oceanic crust. J. Geophys. Res.: Solid Earth 97, 19749–19770.
Rehkämper, M., Halliday, A.N., Fitton, J.G., Lee, D.C., Wieneke, M., Arndt, N.T., 1999. Ir, Ru, Pt, and Pd in basalts and komatiites: new constraints for the geochemical behavior of the platinum-group elements in the mantle. Geochim. Cosmochim. Acta 63, 3915–3934.
Renggli, C.J., Hellmann, J.L., Burkhardt, C., Klemme, S., Berndt, J., Pangritz, P., Kleine, T., 2022. Tellurium isotope fractionation during evaporation from silicate melts. Geochim. Cosmochim. Acta 339, 35–45.
Rose-Weston, L., Brenan, J.M., Fei, Y., Secco, R.A., Frost, D.J., 2009. Effect of pressure, temperature, and oxygen fugacity on the metal-silicate partitioning of Te, Se, and S: implications for earth differentiation. Geochim. Cosmochim. Acta 73, 4598–4615.
Salters, V.J.M., Stracke, A., 2004. Composition of the depleted mantle. Geochem., Geophys., Geosyst. 5, Q05B07.
Shi, L., Lu, W., Kagoshima, T., Sano, Y., Gao, Z., Du, Z., Liu, Y., Fei, Y., Li, Y., 2022. Nitrogen isotope evidence for Earth's heterogeneous accretion of volatiles. Nat. Commun. 13.
Smythe, D.J., Wood, B.J., Kiseeva, E.S., 2017. The S content of silicate melts at sulfide saturation: new experiments and a model incorporating the effects of sulfide composition. Am. Mineral. 102, 795–803.
Sobolev, A.V., Hofmann, A.W., Kuzmin, D.V., Yaxley, G.M., Arndt, N.T., Chung, S.-L., Danyushevsky, L.V., Elliott, T., Frey, F.A., Garcia, M.O., Gurenko, A.A., Kamenetsky, V.S., Kerr, A.C., Krivolutskaya, N.A., Matvienkov, V.V., Nikogosian, I. K., Rocholl, A., Sigurdsson, I.A., Sushchevskaya, N.M., Teklay, M., 2007. The amount of recycled crust in sources of mantle-derived melts. Science 316, 412–417.
Steenstra, E.S., Seegers, A.X., Eising, J., Tomassen, B.G.J., Webers, F.P.F., Berndt, J., Klemme, S., Matveev, S., van Westrenen, W., 2018. Evidence for a sulfur-undersaturated lunar interior from the solubility of sulfur in lunar melts and sulfide-silicate partitioning of siderophile elements. Geochim. Cosmochim. Acta 231, 130–156.
Suer, T.-A., Siebert, J., Remusat, L., Menguy, N., Fiquet, G., 2017. A sulfur-poor terrestrial core inferred from metal–silicate partitioning experiments. Earth Planet. Sci. Lett. 469, 84–97.
Varas-Reus, M.I., Konig, S., Yierpan, A., Lorand, J.P., Schoenberg, R., 2019. Selenium isotopes as tracers of a late volatile contribution to Earth from the outer Solar System. Nat Geosci. 12, 779–782.
Walker, R.J., 2009. Highly siderophile elements in the Earth, Moon and Mars: update and implications for planetary accretion and differentiation. Geochemistry 69, 101–125.
Wang, W., Li, C.-H., Brodholt, J.P., Huang, S., Walter, M.J., Li, M., Wu, Z., Huang, F., Wang, S.-J., 2021. Sulfur isotopic signature of Earth established by planetesimal volatile evaporation. Nat. Geosci. 14, 806–811.
Wang, W., Walter, M.J., Brodholt, J.P., Huang, S., Petaev, M.I., 2023. Chalcogen isotopes reveal limited volatile contribution from late veneer to Earth. Sci. Adv. 9, eadh0670.
Wang, Z., Becker, H., 2013. Ratios of S, Se and Te in the silicate Earth require a volatile-rich late veneer. Nature 499, 328–331.
Wang, Z., Becker, H., 2015a. Abundances of Ag and Cu in mantle peridotites and the implications for the behavior of chalcophile elements in the mantle. Geochim. Cosmochim. Acta 160, 209–226.
Wang, Z., Becker, H., 2015b. Comment on "A non-primitive origin of near-chondritic S–Se–Te ratios in mantle peridotites: implications for the Earth's late accretionary history" by KönigS. Et al. [Earth Planet. Sci. Lett. 385 (2014) 110–121]. Earth Planet. Sci. Lett. 417, 164–166.
Wang, Z., Becker, H., Gawronski, T., 2013. Partial re-equilibration of highly siderophile elements and the chalcogens in the mantle: a case study on the Baldissero and Balmuccia peridotite massifs (Ivrea Zone, Italian Alps). Geochim. Cosmochim. Acta 108, 21–44.
Wood, B.J., Smythe, D.J., Harrison, T., 2019. The condensation temperatures of the elements: a reappraisal. Am. Mineral. 104, 844–856.
Workman, R.K., Hart, S.R., 2005. Major and trace element composition of the depleted MORB mantle. Earth Planet. Sci. Lett. 231, 53–72.
Wykes, J.L., O'Neill, H.S.C., Mavrogenes, J.A., 2015. The effect of FeO on the sulfur content at sulfide saturation (SCSS) and the selenium content at selenide saturation of silicate melts. J Petrol 56, 1407–1424.
Yierpan, A., König, S., Labidi, J., Schoenberg, R., 2019. Selenium isotope and S-Se-Te elemental systematics along the Pacific-antarctic ridge: role of mantle processes. Geochim. Cosmochim. Acta 249, 199–224.
Yierpan, A., König, S., Labidi, J., Schoenberg, R., 2020. Recycled selenium in hot spot–influenced lavas records ocean-atmosphere oxygenation. Science advance 6, eabb6179.
Zhang, Z., Hirschmann, M.M., 2016. Experimental constraints on mantle sulfide melting up to 8 GPa. Am. Mineral. 101, 181–192.